Parameter selection methods for axisymmetric flame tomography through Tikhonov regularization

Emil O. Åkesson[1] and Kyle J. Daun[2,3,*]

[1]Division of Combustion Physics, Lund Institute of Technology, Lund SE-22100, Sweden
[2]Institute for Chemical Process and Environmental Technology, National Research Council of Canada, Ottawa K1A 0R6, Canada
[3]Current address: Department of Mechanical and Mechatronics Engineering, University of Waterloo, Waterloo, Ontario N2L 3G1, Canada

*Corresponding author: kjdaun@mme.uwaterloo.ca

Received 22 August 2007; accepted 24 November 2007;
posted 5 December 2007 (Doc. ID 86755); published 17 January 2008

Deconvolution of optically collected axisymmetric flame data is equivalent to solving an ill-posed problem subject to severe error amplification. Tikhonov regularization has recently been shown to be well suited for stabilizing this deconvolution, although the success of this method hinges on choosing a suitable regularization parameter. Incorporating a parameter selection scheme transforms this technique into a reliable automatic algorithm that outperforms unregularized deconvolution of a smoothed data set, which is currently the most popular way to analyze axisymmetric data. We review the discrepancy principle, L-curve curvature, and generalized cross-validation parameter selection schemes and conclude that the L-curve curvature algorithm is best suited to this problem.

OCIS codes: 120.1740, 120.7000, 280.1740, 280.2470.

1. Introduction

Soot formation plays an important role in the physics of combustion, and accordingly, one must have a good understanding of soot formation and distribution processes when designing and evaluating combustion systems to maximize efficiency and minimize emitted pollutants. Noninvasive optical techniques offer simple and relatively inexpensive means of studying the soot concentration as well as temperature in the latter two cases. In line of sight attenuation (LOSA) experiments [1], for example, soot concentration is inferred from the attenuation of collimated light as it passes through the flame, while in emission/absorption tomography [2] and multicolor pyrometry [3,4] the radial temperature distribution within the flame is inferred from measured soot incandescence. In all three cases, tomographic inverse problems governed by Abel's integral equation [5] must be solved to recover the desired radial property distribution from the optically collected data.

This procedure is complicated by the ill-posed nature of Abel's integral equation [5], which amplifies small perturbations in the data into large errors in the recovered property distribution. Several researchers [6–8] have recently shown that Tikhonov regularization [9–11] can stabilize the inversion of Abel's integral equation, thereby mitigating the effects of this ill-posedness. The amount of regularization is controlled by a continuously variable regularization parameter that represents a trade-off between accuracy and stability. To obtain an accurate solution the regularization parameter must be large enough to suppress perturbation amplification, but not so large as to overwhelm the original governing equations. The regularization parameter is often selected by trial and error [7,11], a labor-intensive process that requires the analyst to have some specialized knowledge of ill-posed problems and inverse analysis. There exist, however, algorithms that automatically analyze the problem and select a suitable regularization parameter based on a variety of different criteria [10,12–15]. By using these methods one can develop a black box algorithm that provides a regularized solution without requiring

0003-6935/08/030407-10$15.00/0

any user input, making it an ideal tool for researchers who do not have a specialized knowledge of inverse analysis. To date, however, there have been no systematic evaluation and comparison of how these parameter selection algorithms perform on the axisymmetric flame deconvolution problem.

The objective of this study is to identify automatic parameter selection algorithms that are well suited to solving axisymmetric flame deconvolution problems. We begin with a brief overview of the ill-posed nature of Abel's integral equation, a summary of onion peeling (OP) and Abel three-point (ATP) deconvolution, and how Tikhonov regularization acts to stabilize these deconvolution techniques. The automatic parameter selection methods are then described in detail, and their performance is assessed by using them to solve two example problems. This analysis shows that Tikhonov regularization is most effective when used to stabilize OP deconvolution, and while all the parameter selection methods perform well, the L-curve curvature criterion appears best suited for this application.

2. Abel's Integral Equation

The axisymmetric flame deconvolution problem is governed by Abel's integral equation, a Volterra integral equation of the first kind [1,2,5]. In combustion applications, it arises when line-of-sight intensity measurements have been made of a flame, and recorded projected data are an integrated property field. Under the assumption that the flame is axisymmetric, the relationship between a one-dimensional projection, $P(x)$, and its corresponding radial property field, $F(r)$, is given by Abel's integral equation

$$P(x) = 2\int_x^R \frac{F(r)r}{\sqrt{r^2 - x^2}}\,\mathrm{d}r, \tag{1}$$

where x is the abscissa coordinate of projected data, r is the radial coordinate of the property field, and R is the flame radius as shown in Fig. 1. In the case of a LOSA experiment, $P(x) = -\ln(I_\lambda(x)/I_{\lambda 0})$ is the spectral intensity attenuation along the chord passing through the flame at x, and $F(r)$ is the radial distribution of absorption coefficients, $\alpha_\lambda^a(r)$. Abel's integral equation has an analytical solution called the Abel transform:

$$F(r) = -\frac{1}{\pi}\int_x^R \frac{P'(x)}{\sqrt{x^2 - r^2}}\,\mathrm{d}x, \tag{2}$$

which includes the derivative of the projected data, $P'(x) = dP(x)/dx$.

In real-world experiments, however, the projected data consist of a discrete set of N values, and accordingly, numerous discretization techniques that transform Abel's integral equation, or its solution, from the continuous domain into the discrete domain have been developed [1]. The most straightforward scheme is OP, in which the flame field is first discretized

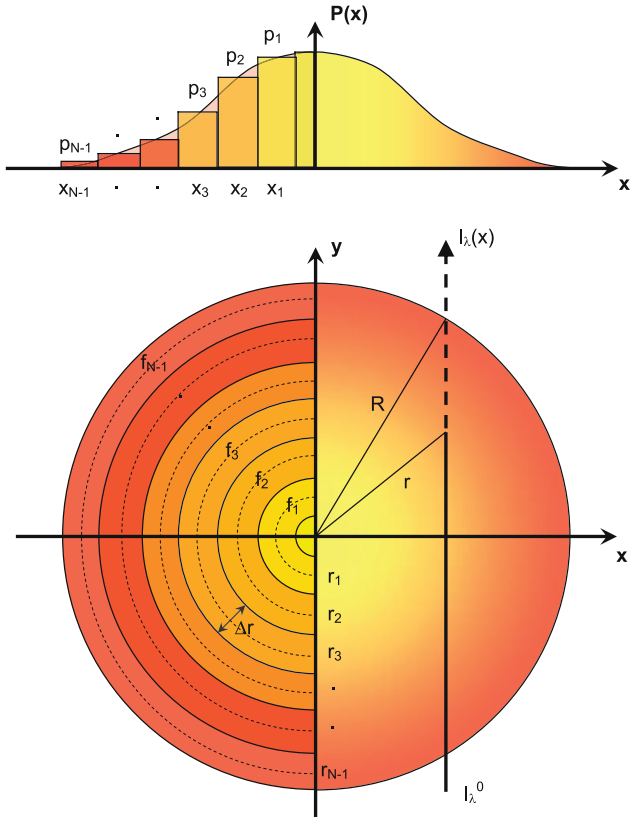

Fig. 1. (Color online) Axisymmetric flame deconvolution geometry.

into N annular elements, each of a width $\Delta r = R/(N - 0.5)$, and $F(r)$ is assumed to hold a constant value over each element as illustrated in Fig. 1. The integral of Eq. (1) is then rewritten as a summation of N integrals, each corresponding to an annular element; since the field distribution is constant over every subdomain it can be extracted from each integral, leaving only the kernel, $r/(r^2 - x^2)^{1/2}$. Carrying out the remaining integral over each annulus results in a matrix equation

$$\mathbf{A}_{\mathrm{OP}}\mathbf{x} = \mathbf{b}, \tag{3}$$

where $\mathbf{b} = \{p_0, p_1, p_2, \ldots, p_{N-1}\}^{\mathrm{T}}$ and $\mathbf{x} = \{f_0, f_1, f_2, \ldots, f_{N-1}\}^{\mathrm{T}}$ are discrete sets of the projected data and the deconvolved field variables evaluated at the center of the annular elements, respectively, and $\mathbf{A}_{\mathrm{OP}}$ contains geometric terms given in [1].

A more sophisticated discretization is given by the ATP technique. This technique again starts by splitting the flame field into N annular elements of uniform thickness. Unlike OP, however, ATP discretizes the Abel transform by fitting the jth projected data values and their two neighboring values with an interpolating quadratic function, $\tilde{P}_j(x)$, that can be differentiated to obtain an approximation for $P'(x)$ over the domain of x that subtends the jth annulus. Writing this equation over every annulus results in another matrix equation:

$$\mathbf{x} = \mathbf{D}_{\mathrm{ATP}}\mathbf{b}, \tag{4}$$

where $\mathbf{D}_{\mathrm{ATP}} = \mathbf{A}_{\mathrm{ATP}}^{-1}$ is the discrete representation of the Abel transform given in [1].

Recovering $\mathbf{x}$ is complicated by the fact that both Eqs. (3) and (4) are mathematically ill-posed. The concept of ill-posed problems arose from Hadamard's criteria for a well-posed problem [16,10], i.e., well-posed problems (i) have a solution that is (ii) unique and (iii) a continuous function of the input data. While the existence and uniqueness of a solution to Abel's integral equation can be proved mathematically, [5] thereby guaranteeing that criteria (i) and (ii) are satisfied, Abel's integral equation is ill-posed because its solution, $F(r)$, is highly sensitive to small perturbations in the projected data, $P(x)$. This characteristic stems from the fact that, as N increases, the jth row of $\mathbf{A}$ corresponding to the jth annulus more closely resembles its neighboring rows, and consequently $\mathbf{A}$ becomes increasingly ill-conditioned (rank deficient) and approaches singularity as N tends to infinity. (The singular problem has an infinite number of solutions, whereas an ill-conditioned problem has only one.) The degree of error amplification depends on the curvature of $\|\mathbf{Ax} - \mathbf{b}\|_2^2$, which in turn is directly related to the condition number of $\mathbf{A}$:

$$\frac{\|\boldsymbol{\delta}\mathbf{x}\|}{\|\mathbf{x}\|} \leq \|\mathbf{A}\| \cdot \|\mathbf{A}^{-1}\| \frac{\|\boldsymbol{\delta}\mathbf{b}\|}{\|\mathbf{b}\|} = \mathrm{Cond}(\mathbf{A}) \frac{\|\boldsymbol{\delta}\mathbf{b}\|}{\|\mathbf{b}\|}. \tag{5}$$

Since the interpolating quadratic functions used in ATP represent $P(x)$ as a smoothly varying function and are usually derived assuming radial symmetry, i.e., $dP/dx\,|_{x=0} = 0$, ATP incorporates more information about the projected data than OP does, which makes no such implicit assumptions about the character of $P(x)$ or $F(r)$. As a result $\mathrm{Cond}(\mathbf{A}_{\mathrm{ATP}}) < \mathrm{Cond}(\mathbf{A}_{\mathrm{OP}})$ at a given value of N [7], so ATP is generally more resilient to this error amplification compared to OP [1], and consequently ATP is generally preferred by combustion experimentalists [1].

Unfortunately, neither OP nor ATP address the underlying ill-posedness of Abel's integral equation directly. Instead, it is more common to pretreat the projected data with a smoothing algorithm before tomographic inversion. A popular way to do this is through local regression smoothing (LOESS) [17], in which a smoothed projected data set is created by replacing each original error-contaminated data point with a weighted average of a certain number, or span, of neighboring data points. The choice of span is made visually by the experimentalist based on experience and expectation of the final result, which compromises the scientific reproducibility of the deconvolved data. More importantly, this technique does not treat the ill-posedness of the tomographic problem directly, but merely its symptoms.

3. Tikhonov Regularization

An efficient way of dealing with the ill-posed nature of this problem directly is Tikhonov regularization [9,10], a process that replaces the original ill-posed problem with an approximate but less ill-posed problem. In this technique, the original matrix equation is augmented with extra rows that enforce a smoothness criterion,

$$\begin{bmatrix} \mathbf{A} \\ \lambda\mathbf{L} \end{bmatrix} \mathbf{x} = \begin{bmatrix} \mathbf{b} \\ 0 \end{bmatrix}, \tag{6}$$

where $\mathbf{L}$ is a smoothing matrix and the regularization parameter λ controls the extent of regularization. Setting $\mathbf{L}$ equal to a discrete approximation of the ∇-operator,

$$\mathbf{L} = \begin{bmatrix} 1 & -1 & 0 & \cdots & 0 \\ 0 & 1 & -1 & & \vdots \\ \vdots & & \ddots & \ddots & 0 \\ 0 & \cdots & 0 & 1 & -1 \end{bmatrix} \tag{7}$$

has been shown to work particularly well for problems governed by diffusion-driven processes and thus have naturally smooth solutions, which is the case for laminar flames [7]. Since Eq. (6) is overdetermined, the regularized solution to the problem is the vector $\mathbf{x}_\lambda$ that minimizes the residual norm of the augmented matrix equation, i.e.,

$$\mathrm{Min}_x\left(\|\mathbf{Ax} - \mathbf{b}\|_2^2 + \lambda^2\|\mathbf{Lx}\|_2^2\right). \tag{8}$$

In a topographical sense, adding $\lambda^2\|\mathbf{Lx}\|_2^2$ to the residual norm steepens the residual function in the vicinity of the solution. Increasing the regularization parameter reduces perturbation amplification resulting in improved precision but decreases the influence of the original ill-conditioned matrix, impairing solution accuracy. Graphic examples of this effect are presented in [7] and [10].

Although $\mathbf{x}_\lambda$ can be found by solving the normal equations derived from the residual norm, a preferred approach is to perform a singular value decomposition (SVD) on the augmented matrix [11]. In SVD, the $(N \times N)$ $\mathbf{A}$ matrix is decomposed so that

$$\mathbf{A} = \mathbf{U}\boldsymbol{\Sigma}\mathbf{V}^T = \sum_{i=1}^{N} \mathbf{u}_i \boldsymbol{\sigma}_i \boldsymbol{v}_i^T, \tag{9}$$

where $\mathbf{U}$ and $\mathbf{V}$ consist of N orthonormal column vectors, $\mathbf{u}_i$ and $\boldsymbol{v}_i$, which are the singular vectors of $\mathbf{A}$, and $\boldsymbol{\Sigma}$ is a diagonal matrix containing the singular values of $\mathbf{A}$, $\boldsymbol{\sigma}_i$. Due to the orthogonality of $\mathbf{U}$ and $\mathbf{V}$ the solution to $\mathbf{Ax} = \mathbf{b}$ can be written explicitly in terms of the decomposed elements of $\mathbf{A}$:

$$\mathbf{x} = \sum_{i=1}^{N} \frac{\mathbf{u}_i^T\mathbf{b}}{\boldsymbol{\sigma}_i} \boldsymbol{v}_i = \sum_{i=1}^{N} \left(\frac{\mathbf{u}_i^T\mathbf{b}_0}{\boldsymbol{\sigma}_i} \boldsymbol{v}_i + \frac{\mathbf{u}_i^T\boldsymbol{\delta}\mathbf{b}}{\boldsymbol{\sigma}_i} \boldsymbol{v}_i \right), \tag{10}$$

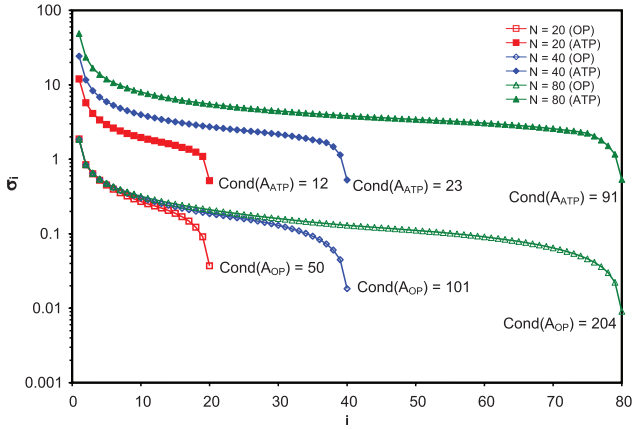

Fig. 2. (Color online) Singular values and condition numbers for OP and ATP matrices.

where $\mathbf{b}$, $\mathbf{b}_0$, and $\boldsymbol{\delta}\mathbf{b}$ contain the perturbed projected data, the unperturbed data, and the perturbations, respectively, so that $\mathbf{b} = \mathbf{b}_0 + \boldsymbol{\delta}\mathbf{b}$. From this equation it is clear that error amplification is caused by small singular values, and indeed Cond($\mathbf{A}$) can be alternatively expressed as the ratio of maximum and minimum singular values. Figure 2 shows the singular value spectra of the OP and ATP matrices generated using different values of N, which confirms that the singular values are indeed very small for both matrices and become progressively smaller as N increases, an effect that is more pronounced for OP matrices.

While SVD is a valuable tool for diagnosing ill-conditioned matrices, it can also be used to find the vector $\mathbf{x}_\lambda$ that minimizes the residual of Eq. (6); the extra $N - 1$ rows of the augmented matrix correspond to $N - 1$ null singular values, and the corresponding terms are excluded from the summation in Eq. (10).

4. Selecting the Regularization Parameter

The key to successful Tikhonov regularization lies in choosing a regularization parameter that is just large enough to stabilize the inversion against perturbation amplification but not so large as to overwhelm the original governing equations in $\mathbf{A}$ with the smoothing matrix, $\lambda\mathbf{L}$. The optimal regularization parameter, λ^*, minimizes the total error, $\varepsilon_{\text{tot},\lambda}$, equal to the sum of the error due to perturbation amplification, $\varepsilon_{\text{pert},\lambda}$, and the error caused by regularization $\varepsilon_{\text{reg},\lambda}$. This is given by [10]

$$\varepsilon_{\text{tot},\lambda} \le \varepsilon_{\text{pert},\lambda} + \varepsilon_{\text{reg},\lambda} = \|\mathbf{A}_\lambda^{-1}\boldsymbol{\delta}\mathbf{b}\|_2 + \|(\mathbf{A}^{-1} - \mathbf{A}_\lambda^{-1})\mathbf{b}_0\|_2, \tag{11}$$

where $\mathbf{A}^{-1}$ is the pseudoinverse of $\mathbf{A}$, and $\mathbf{A}_\lambda^{-1}$ is the regularized pseudoinverse, defined implicitly as $\mathbf{x}_\lambda = \mathbf{A}_\lambda^{-1}\mathbf{b}$. [Note that $\varepsilon_{\text{tot},\lambda}$ is defined relative to the solution of the unperturbed and unregularized matrix equation $\mathbf{x} = \mathbf{A}^{-1}\mathbf{b}_0$ and not the continuous field variable distribution $F(r)$; errors arising from discretizing Eqs. (1) and (2) lie beyond the scope of regularization.]

Finding a near-optimal regularization parameter is far from straightforward, since it is difficult to separate the exact, physically meaningful, projected data from the noise, unknown in both amount and correlation, as well as from the discretization error. While some researchers advocate a trial-and-error approach [7,11] for selecting the regularization parameter, others have developed parameter selection algorithms that choose λ automatically. These algorithms provide good regularization parameters more efficiently and reliably than trial and error and can also be used in a black box deconvolution algorithm that requires no specialized knowledge of inverse analysis on the part of the user. In many of these strategies $\varepsilon_{\text{tot},\lambda}$ is minimized approximately by finding the value of λ that sets $\varepsilon_{\text{reg},\lambda} \approx \varepsilon_{\text{pert},\lambda}$, since the former increases monotonically with λ, while the latter decreases monotonically. Three of the most popular parameter selection methods are summarized below; a more thorough review is provided by Hansen [10].

A. Discrepancy Principle

The discrepancy principle (DP), due to Morozov [12], is based on the reasoning that the least-squares residual, $\|\mathbf{A}\mathbf{x}_\lambda - \mathbf{b}\|_2$, should be at least the same order of magnitude as the noise, and that the selected regularization parameter thereof should be as large as possible [12,18]. This means solving

$$\|\mathbf{A}\mathbf{x}_\lambda - \mathbf{b}\|_2 = \delta \approx \|\boldsymbol{\delta}\mathbf{b}\|_2, \tag{12}$$

where δ is an estimated upper bound of the noise contamination. A good estimate for δ is the standard error of replicated projected data measurements, assuming they are contaminated with unbiased error. Multiplying the vectors inside the norms of Eq. (12) by $\mathbf{A}_\lambda^{-1}$ shows that the DP roughly satisfies $\varepsilon_{\text{reg},\lambda} \approx \varepsilon_{\text{pert},\lambda}$. Note that the selected regularization parameter will go to zero as the level of error contamination goes to zero, a desirable attribute not found in selection criteria that do not rely on explicit estimates of δ to find λ [19,20].

B. L-Curve Criterion

A more recent strategy for selecting the regularization parameter is the L-curve criterion (LCC) of Hansen and O'Leary [13]. In this approach the regularization parameter is chosen using the L-curve, which is formed by plotting the two norms of the Tikhonov objective function $\|\mathbf{L}\mathbf{x}_\lambda\|_2^2$ versus $\|\mathbf{A}\mathbf{x}_\lambda - \mathbf{b}\|_2^2$ over the range of possible λ values on a log–log scale as shown in Fig. 3. The vertical part of the L-curve can be isolated by plotting the L-curve with a projection consisting entirely of noise, whereas the horizontal part can be formed by plotting the L-curve with a projection devoid of noise [13]. Solutions corresponding to the vertical part of the L-curve are thus dominated by noise, while those on the horizontal part are overregularized, and a good trade-off between $\varepsilon_{\text{pert},\lambda}$ and $\varepsilon_{\text{reg},\lambda}$ is intuitively found at the corner of the L-curve, where the vertical and horizon-

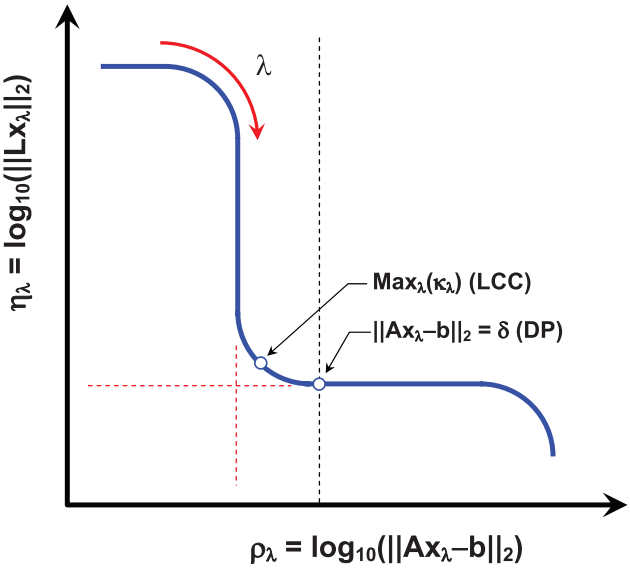

Fig. 3. (Color online) L-curve.

tal parts meet. The distinctiveness of the L-curve corner depends on the relative magnitudes of the two norms and thus the magnitude of the noise and the condition number of the **A**-matrix. This is intuitively supported by reasoning that a larger condition number more effectively accentuates the noise and thus more clearly distinguishes it from the rest of the data.

The L-curve corner can be located in a number of ways, the simplest being to plot the L-curve and identify the corner by inspection [7], but this clearly does not constitute an automatic parameter selection method. (Note that the L-curve is defined incorrectly in [7].) A more rigorous technique is to calculate the point of maximum curvature using nonlinear programming. The L-curve curvature, κ_λ, is defined by

$$\kappa_\lambda = \frac{\rho'_\lambda \eta''_\lambda - \rho''_\lambda \eta'_\lambda}{[(\rho'_\lambda)^2 + (\eta'_\lambda)^2]^{3/2}}, \tag{13}$$

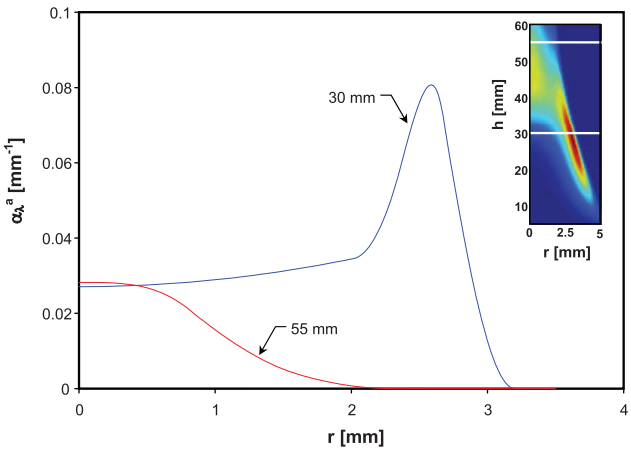

Fig. 4. (Color online) Field distributions of the absorption coefficient at 30 and 55 mm above the burner [3].

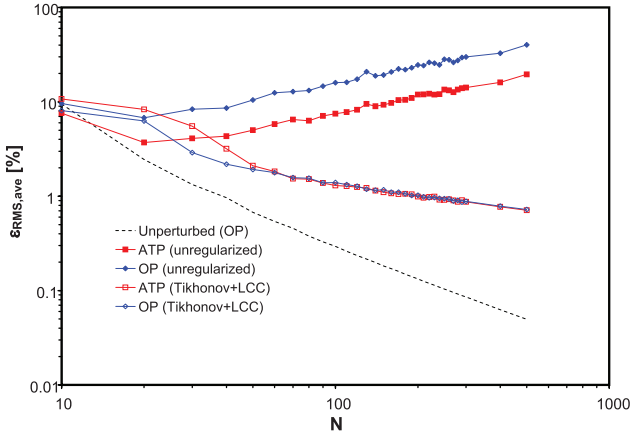

Fig. 5. (Color online) Accuracy of unregularized versus regularized solutions found using parameter selection methods for the 30 mm profile.

where $\rho_\lambda = \log_{10}(\|\mathbf{A}\mathbf{x}_\lambda - \mathbf{b}\|_2)$ and $\eta_\lambda = \log_{10}(\|\mathbf{L}\mathbf{x}_\lambda\|_2)$, and all derivatives are with respect to λ. The first- and second-order derivatives can be approximated using finite differences, although the generalized singular value decomposition (SVD) technique described in [10] offers a more efficient and elegant way of calculating these quantities.

The LCC is closely related to the DP; Hansen [10] shows that the solution $\mathbf{x}_\lambda$ that satisfies Eq. (13) corresponds to a point where the L-curve is intercepted by a vertical line corresponding to $\|\mathbf{A}\mathbf{x}_\lambda - \mathbf{b}\|_2 = \delta$ passing through the ρ_λ axis as shown in Fig. 3. The solution obtained by the DP is located to the right of the L-curve corner, which itself is located approximately at $\|\mathbf{A}\mathbf{A}_\lambda^{-1}\delta\mathbf{b} - \mathbf{b}\|_2$ on the ρ_λ axis [10], and consequently the DP consistently provides a more conservative value of λ than the LCC does. In the compensated DP [10,15] the right-hand side of Eq. (13) is divided by $\|\mathbf{I} - \mathrm{Tr}(\mathbf{A}\mathbf{A}_\lambda^{-1})\|_2$ to account for the fact that regularization decreases the number of de-

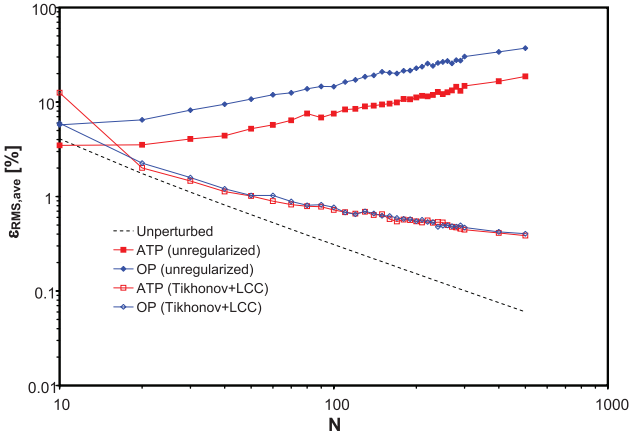

Fig. 6. (Color online) Accuracy of unregularized versus regularized solutions found using parameter selection methods for the 55 mm profile.

grees of freedom of the regularized matrix equation, although this modification is not implemented here.

Although the LCC is perhaps the most intuitive parameter selection method, it has several shortcomings. If the solution is very smooth or very rough, the L-curve corner may not be a good approximation of the optimal regularization parameter [19,21], and under certain circumstances the L-curve may not necessarily possess a distinct corner at all [22]. The incomplete mathematical understanding of these phenomena highlights the fundamental heuristic nature of the LCC. Nevertheless, Wu [8] advocates this technique for performing Tikhonov-regularized axisymmetric flame deconvolution.

C. Generalized Cross Validation

Generalized cross validation (GCV) [14,15] is derived from the ordinary cross-validation technique developed by Allen [23], which strives to identify a value of λ that makes $[\mathbf{A}\mathbf{x}_\lambda^k]_k$ a good estimate of the kth element of $\mathbf{b}$, b_k, where $\mathbf{x}_\lambda^k$ is the regularized solution of $\mathbf{A}\mathbf{x} = \mathbf{b}$ with the kth row omitted. This condition is satisfied by the value of λ that minimizes the prediction of sum of squares (PRESS) objective function [23]

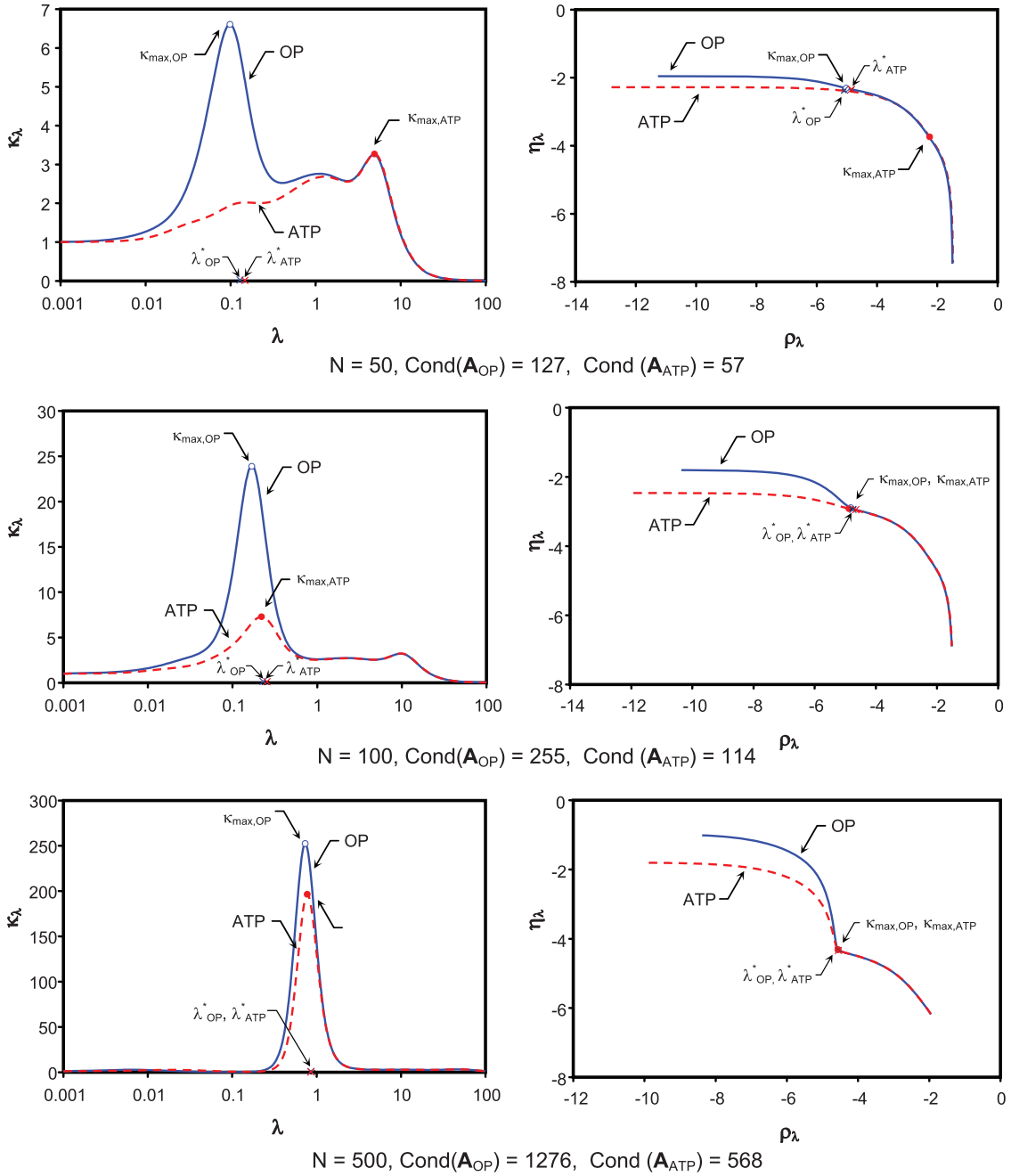

Fig. 7. (Color online) L-curves and L-curve curvatures for problems having different condition numbers, for the 30 mm profile contaminated with Gaussian noise, $\sigma = 0.01 p_{max}$. (Solid and dashed curves represent OP and ATP, respectively.)

$$V(\lambda) = \frac{1}{N}\sum_{i=1}^{N}\left([\mathbf{A}\mathbf{x}_\lambda^k]_k - b_k\right)^2, \tag{14}$$

which through the Sherman–Morrison–Woodbury formula [23] is equivalent to

$$V(\lambda) = \|\mathbf{B}_\lambda(\mathbf{I} - \mathbf{A}\mathbf{A}_\lambda^{-1})\mathbf{b}\|_2^2, \tag{15}$$

where $\mathbf{B}_\lambda$ is a diagonal matrix with $B_{\lambda,kk} = 1/(1 - [\mathbf{A}\mathbf{A}_\lambda^{-1}]_{kk})$.

While the general philosophy of ordinary cross validation is sound, accurate prediction of b_k is elusive if $\mathbf{A}$ is strongly diagonally dominant. Golub *et al.* [14] show through SVD that a more robust estimate of λ is found by minimizing the rotation-invariant version of Eq. (15):

$$G(\lambda) = \frac{\|(\mathbf{I} - \mathbf{A}\mathbf{A}_\lambda^{-1})\mathbf{b}\|_2^2}{\mathrm{Tr}(\mathbf{I} - \mathbf{A}\mathbf{A}_\lambda^{-1})^2} = \frac{\|\mathbf{A}\mathbf{x}_\lambda - \mathbf{b}\|_2^2}{\mathrm{Tr}(\mathbf{I} - \mathbf{A}\mathbf{A}_\lambda^{-1})^2}. \tag{16}$$

Although Eq. (16) is best interpreted as a variation of the PRESS objective function, it can also be related to the L-curve. The product $\mathbf{A}\mathbf{A}_\lambda^{-1}$ is also sometimes called the influence matrix [10] and its deviation from the identity matrix characterizes $\varepsilon_{\mathrm{reg}}(\lambda)$, which is a slowly increasing function of λ, and as noted above, $\mathrm{Tr}(\mathbf{I} - \mathbf{A}\mathbf{A}_\lambda^{-1})$ is a measure of the number of degrees of freedom. By minimizing Eq. (16), then, one is effectively determining the point at which $\|\mathbf{A}\mathbf{x}_\lambda - \mathbf{b}\|_2$ transforms from a slowly varying function to a rapidly increasing function of λ, which roughly corresponds to the L-curve corner [10].

Cross validation is predicated on the assumption that the data are contaminated by uncorrelated noise, and consequently GCV performs poorly on problems with highly correlated noise [10,15]. (Fortunately, the noise contaminating optical data from most axisymmetric flame experiments is predominantly uncorrelated.) Also, the minimum of $G(\lambda)$ is notoriously weak, making it numerically difficult to locate [10,14], although it becomes stronger as N and Cond($\mathbf{A}$) increase [15].

5. Axisymmetric Flame Deconvolution Test Problems

The performance of the regularization parameter choice methods are evaluated on a LOSA test problem inspired by the absorption coefficient from an ethylene laminar coflow diffusion flame [3]. The test profiles correspond to radial distributions measured at 30 and 55 mm above the burner.

Smooth field variable distributions are obtained by fitting experimental data points with continuous piecewise polynomials that obey $F'(r) = 0$, to enforce radial symmetry, and $F(R) = 0$, as seen in Fig. 4. Each point in the unperturbed projected data set is derived by integrating

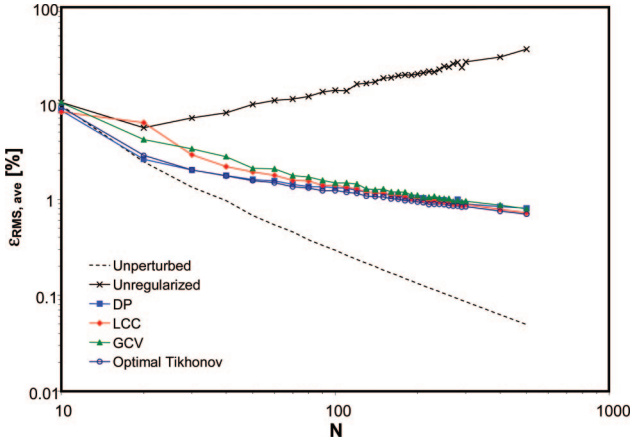

Fig. 8. (Color online) Accuracy of Tikhonov-regularized solutions found using parameter selection methods for the 30 mm profile.

$$P_i = P(x_i) = -\ln\left(\frac{I_\lambda}{I_\lambda^0}\right) = \int_{S_i}\alpha_\lambda^a(s)\,\mathrm{d}s = \int_x^R \frac{\alpha_\lambda^a(r)r}{\sqrt{r^2 - x_i^2}}\,\mathrm{d}r \tag{17}$$

analytically and are then contaminated with an error sampled from an unbiased Gaussian distribution having a standard deviation σ, expressed as a percentage of the maximum value of $P(x)$, $P_{\max}$. (Unless otherwise stated, $\sigma = 0.01P_{\max}$.) This treatment models the error contamination commonly encountered under experimental conditions [3]. Once a solution is recovered from the projected data, its accuracy is quantified by its root-mean-square error,

$$\varepsilon_{\mathrm{rms}} = \frac{\|\mathbf{f} - \mathbf{f}_{\mathrm{exact}}\|_2}{\sqrt{N}\cdot\mathrm{Max}(\mathbf{f}_{\mathrm{exact}})}, \tag{18}$$

where each element of $\mathbf{f}_{\mathrm{exact}}$ contains $F(r)$ evaluated at the center of the corresponding annular element, and the magnitude of the largest element, Max($\mathbf{f}_{\mathrm{exact}}$), is used to nondimensionalize the error.

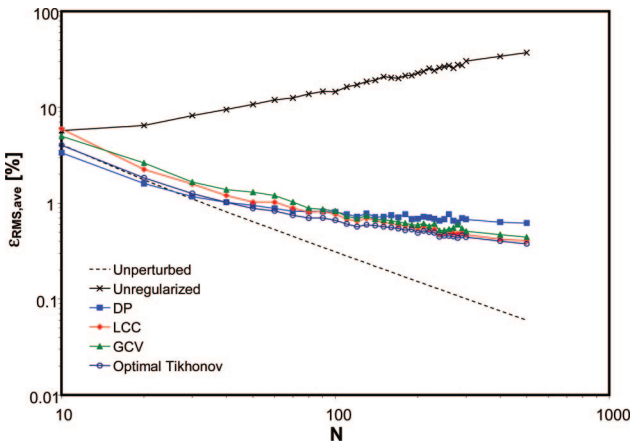

Fig. 9. (Color online) Accuracy of Tikhonov-regularized solutions found using parameter selection methods for the 55 mm profile.

In the parameter selection methods described above, the recovered regularization parameter is either a root or an extremum of a univariate function. In this implementation these problems are solved using a golden section search algorithm [24].

The parameter selection methods are first applied to solve the matrix equations derived from OP and ATP deconvolution. (Tikhonov regularization can only be applied on a problem of the form $\mathbf{Ax} = \mathbf{b}$, so $\mathbf{A}_{\mathrm{ATP}}$ was derived by inverting $\mathbf{D}_{\mathrm{ATP}}$ using SVD.) Figures 5 and 6 show the average $\varepsilon_{\mathrm{rms}}$ for field distributions obtained from 50 independent projected data sets and plotted versus N. The root-mean-square error of the unperturbed (OP) solution increases with N, since the discretization error drops as Δr grows small. This is not so if the projected data are contaminated with experimental error, however, since both $\mathbf{A}_{\mathrm{ATP}}$ and $\mathbf{A}_{\mathrm{OP}}$ become progressively ill-conditioned as N increases. Since $\mathrm{Cond}(\mathbf{A}_{\mathrm{ATP}})$ is consistently lower than $\mathrm{Cond}(\mathbf{A}_{\mathrm{OP}})$, error amplification due to ATP deconvolution is not as severe as for OP.

Figures 5 and 6 also show that when Tikhonov regularization is applied using the LCC to choose λ, the error again drops with increasing N, demonstrating that Tikhonov regularization suppresses the ill-conditioning of both $\mathbf{A}_{\mathrm{OP}}$ and $\mathbf{A}_{\mathrm{ATP}}$. Interestingly, when regularization is used to stabilize deconvolution, the solutions obtained using OP are generally more accurate than those found through ATP, particularly for smaller values of N. This somewhat counterintuitive result is explained in Fig. 7, which shows that, when $\mathrm{Cond}(\mathbf{A})$ is small, the L-curve cor-

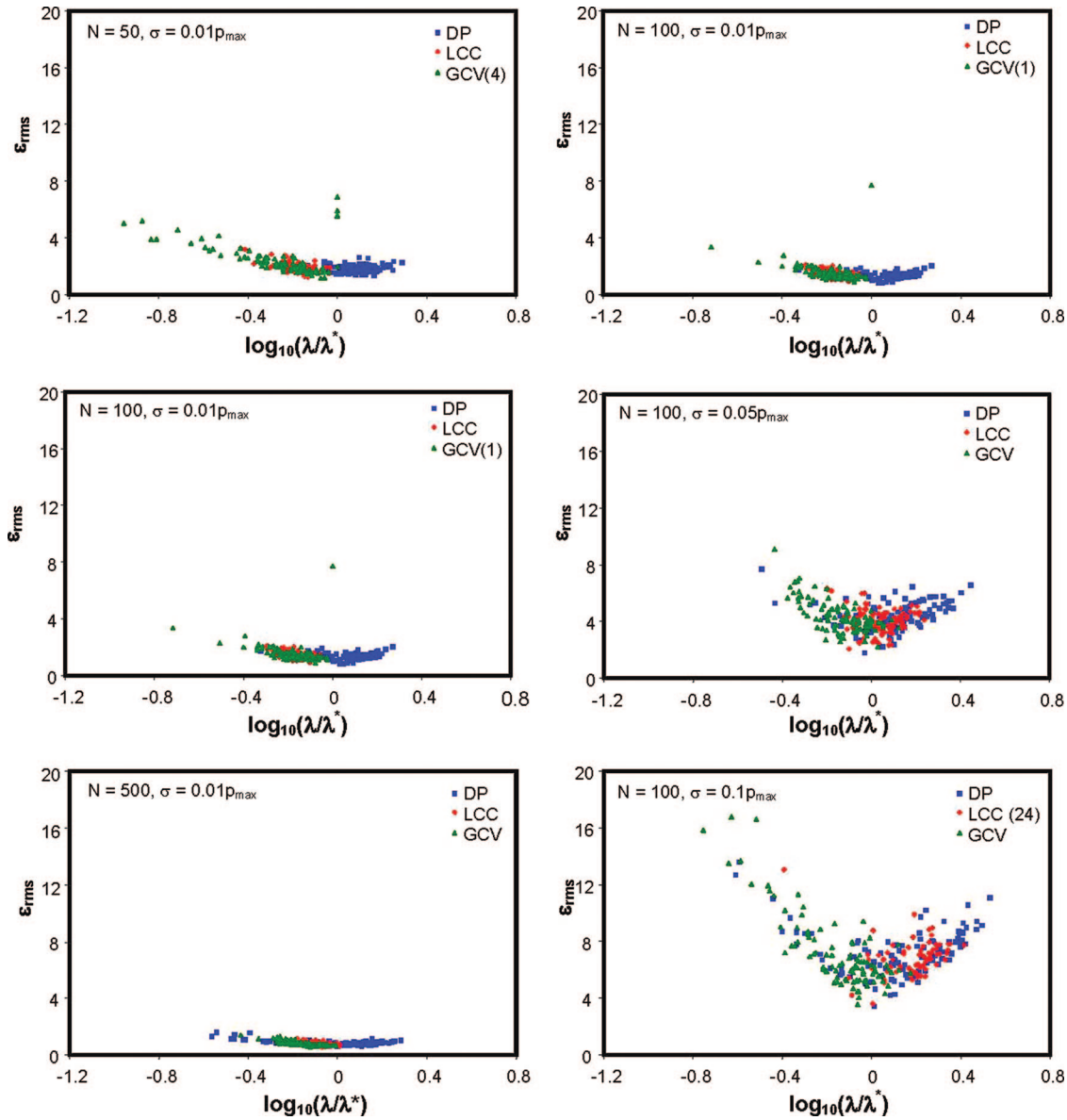

Fig. 10. (Color online) Scatterplots showing the root-mean-square errors of recovered solutions for different quadratures (left) and noise levels (right), relative to regularization parameters normalized by the optimal regularization parameter for the 30 mm profile. Numbers in parentheses denote the instances when a regularization parameter was not found.

ner is indistinct and does not correspond to the location of maximum curvature for the ATP case with $N = 50$. The curvature increases with Cond($\mathbf{A}$), which makes the value of λ corresponding to the L-curve corner more distinct and easier to find. In all cases the L-curve corner lies close to the optimal regularization parameter, λ^*, that minimizes $\|\mathbf{x}_\lambda - \mathbf{A}_{OP}{}^{-1} - \mathbf{b}_0\|_2{}^2$. (Note that $\mathbf{A}_{OP}^{-1}\mathbf{b}_0$ is usually inaccessible, since $\mathbf{b}_0$ cannot normally be distinguished from $\mathbf{b} = \mathbf{b}_0 + \delta\mathbf{b}$, but this solution is useful to establish the maximum performance that can be obtained from a parameter-choice method.)

In other words, Tikhonov regularization is most effective in problems where Cond($\mathbf{A}$) is large, which is why OP generally performs better than ATP when Tikhonov regularization is used to stabilize the deconvolution process and, along with diminishing the discretization error, is also why Tikhonov solution accuracy improves as N increases. (This argument also applies to the DP and GCV.) Accordingly, the remaining discussion is limited to examining the performance of parameter selection methods on OP.

Figures 8 and 9 show the accuracy of Tikhonov-regularized solutions obtained using the LCC, DP, and GCV parameter choice methods, along with that of the solution obtained using the optimal regularization parameter λ^*. In the 30 mm profile case the solutions recovered via the DP are more accurate than the LCC and GCV solutions at small values of N, and the accuracy of all three techniques converge to that of the optimal case as N becomes large. The same trends are observed in the 55 mm profile case, although the DP solutions become less accurate relative to the LCC, GCV, and optimal Tikhonov solutions at higher resolutions.

Further insight into the relative performance of the parameter-choice methods is gained from scatter-plots of the root-mean-square error of 100 independent deconvolved distributions against $\log_{10}(\lambda/\lambda^*)$ shown in Fig. 10. The position of a solution relative to the horizontal axis shows how far the value of λ obtained from the parameter-choice algorithm deviates from λ^*, while the vertical position shows how this deviation impacts solution accuracy. The left side of Fig. 10 shows plots obtained with $\sigma = 0.01P_{max}$ and $N = 50$, 100, and 500. In general, the recovered regularization parameters group closer to λ^*, and ε_{RMS} values become smaller as N and Cond($\mathbf{A}$) increase, which is consistent with the theory described above; this effect is most prominent for the GCV and LCC cases compared to the DP. The DP tends to provide regularization parameters slightly larger than λ^*, as expected, while GCV underregularizes and the LCC regularization parameters are distributed evenly around λ^*. There is little difference in the accuracy of the recovered solutions, however, particularly at large values of N. Note that in a number of cases (denoted parenthetically) the golden section search failed to find the minimizer for Eq. (16) due to the shallowness of the GCV objective function, particularly at small values of N.

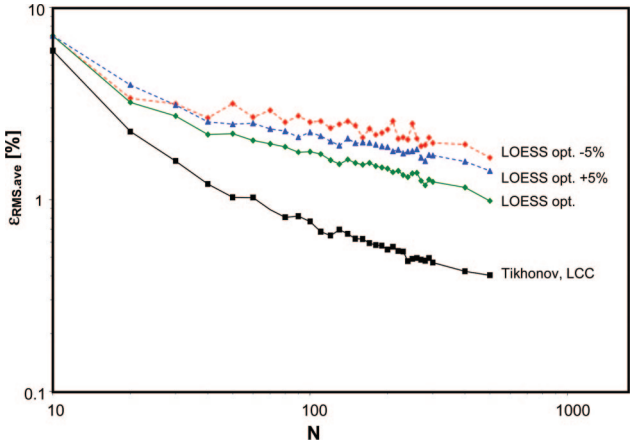

Fig. 11. (Color online) Comparison of Tikhonov solutions obtained using regularization and solutions obtained using unregularized ATP deconvolution with LOESS presmoothing of projection data for the 30 mm profile.

The right side of Fig. 10 shows plots obtained with $N = 100$ and $\sigma = 1\%$, 5%, and 10% of P_{max}. As one would expect, the degree of deviation from λ^* and ε_{rms} both increase with the level of error contamination in the projected data. The solutions obtained by the LCC appear to be slightly more precise and accurate than those found from the DP and GCV, except at the highest level of error contamination in which case the golden section search algorithm repeatedly identified a local maxima of K_λ to the left of the one corresponding to the L-curve corner, resulting in severely underregularized solutions.

Finally, Figs. 11 and 12 compare the accuracy of solutions obtained using Tikhonov-regularized OP deconvolution to those found from unregularized ATP deconvolution with LOESS presmoothing of the projected data, which is a common practice for analyzing optical data from axisymmetric flames. The Tikhonov regularization parameter is obtained using the LCC, while the optimal LOESS span is found by minimizing

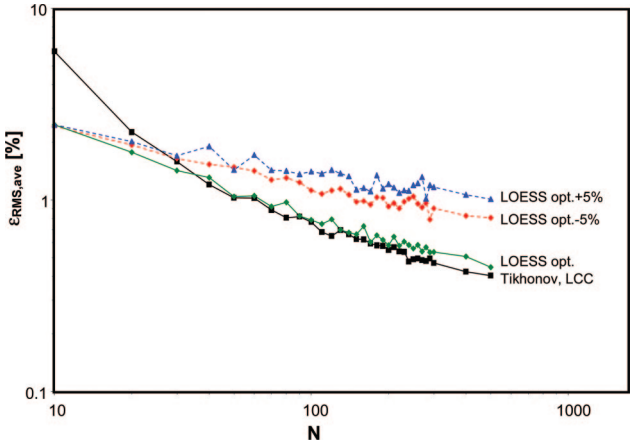

Fig. 12. (Color online) Comparison of Tikhonov solutions obtained using regularization and solutions obtained using unregularized ATP deconvolution with LOESS presmoothing of projection data for the 55 mm profile.

the difference between $F(r)$ and the LOESS solution for each deconvolution. (Just as for λ^* the optimal LOESS span is normally inaccessible, since $\mathbf{b}_0$ is usually unknown, but this solution establishes the maximum accuracy obtainable by presmoothing the data.) To reflect the true heuristic nature of selecting the LOESS-averaging span, the root-mean-square error of solutions obtained using spans 5% smaller and larger than the optimal span are also plotted. The results in Figs. 11 and 12 show that Tikhonov-stabilized deconvolution generally provides more reliable and accurate solutions to axisymmetric flame deconvolution problems compared with unregularized ATP inversion coupled with LOESS presmoothing.

6. Conclusions

We have shown how Tikhonov regularization can stabilize deconvolution of optical data collected from axisymmetric flames. For this procedure to be successful it is paramount to select a suitable regularization parameter that is large enough to suppress noise amplification but not so large as to obscure the governing equations. Although this step can be done manually by trial and error, parameter selection algorithms have been developed that choose a regularization parameter automatically. We have examined the DP, the LCC, and GCV schemes. Coupling one of these techniques with Tikhonov-stabilized regularization results in an automated algorithm that provides more consistent and reproducible results in a timelier manner compared with regularization by trial and error. Furthermore, no specialized knowledge of inverse analysis is required on the part of the analyst, making it an ideal tool for the combustion community.

This technique was demonstrated and the performance of the parameter selection algorithms was evaluated by solving deconvolution test problems derived from a laminar-diffusion flame experiment. The accuracy of regularized solutions improve as the problem becomes progressively ill-posed, which means that Tikhonov regularization should be coupled with OP and performs best at high quadrature, which contrasts with unregularized deconvolution, where ATP deconvolution is generally preferred to OP and experimental resolution is severely limited by the ill-conditioning of the deconvolution matrix. The performance of the parameter selection techniques is similar, although the DP tends to overregularize the problem, and GCV occasionally fails due to the shallowness of its global minimum. For these reasons we recommend the LCC for this application although care must be taken to address the possibility of L-curve curvature multimodality at extremely high levels of error contamination. Finally, a comparison of the accuracy of solutions obtained through Tikhonov-stabilized OP of unsmoothed data and those found by unregularized ATP inversion of data smoothed using LOESS verifies that Tikhonov regularization is a better way to deconvolve axisymmetric flame data compared with the currently popular practice of data presmoothing.

References

1. C. J. Dasch, "One-dimensional tomography: a comparison of Abel, onion-peeling, and filtered backprojection methods," Appl. Opt. **31,** 1146–1152 (1992).
2. R. J. Hall and P. A. Bonczyk, "Sooting flame thermometry using emission/absorption tomography," Appl. Opt. **29,** 4590–4598 (1990).
3. D. R. Snelling, K. A. Thomson, G. J. Smallwood, and Ö. L. Gülder, "Two-dimensional imaging of soot volume fraction in laminar diffusion flames," Appl. Opt. **38,** 2478–2485 (1999).
4. F. Cignoli, S. De Luliis, V. Manta, and G. Zizak, "Two-dimensional two-wavelength emission technique for soot diagnostics," Appl. Opt. **40,** 5370–5378 (2001).
5. R. Gorenflo and S. Vessella, *Abel Integral Equations: Analysis and Applications* (Springer, 1993).
6. J. P. Holloway, S. Shannon, S. M. Sepke, and M. L. Brake, "A reconstruction algorithm for a spatially resolved plasma optical emission spectroscopy sensor," J. Quant. Spectrosc. Radiat. Transfer **68,** 101–115 (2001).
7. K. J. Daun, K. A. Thomson, F. Liu, and G. J. Smallwood, "Deconvolution of axisymmetric flame properties using Tikhonov regularization," Appl. Opt. **45,** 4638–4646 (2006).
8. C. Wu, Department of Chemical Engineering, Tsinghua University, Beijing, China (personal communication, 2007).
9. A. N. Tikhonov and V. A. Arsenin, *Solution of Ill-Posed Problems* (Winston & Sons, 1977).
10. P. C. Hansen, *Rank-Deficient and Discrete Ill-Posed Problems: Numerical Aspects of Linear Inversion* (SIAM, 1998).
11. W. H. Press, S. A. Teukolsky, W. T. Vetterling, and B. P. Flannery, *Numerical Recipes in C: The Art of Scientific Computing,* 2nd ed. (Cambridge U. Press, 1992).
12. V. A. Morozov, "On the solution of functional equations by the method of regularization," Sov. Math. Dokl. **7,** 414–417 (1966).
13. P. C. Hansen and D. P. O'Leary, "The use of the L-curve in the regularization of discrete ill-posed problems," SIAM J. Sci. Comput. (USA) **14,** 1487–1503 (1993).
14. G. H. Golub, M. Heath, and G. Wahba, "Generalized cross-validation as a method for choosing a good ridge parameter," Technometrics **21,** 215–223 (1979).
15. G. Wahba, *Spline Models for Observational Data* (SIAM, 1990).
16. J. Hadamard, *Lectures on Cauchy's Problem in Linear Differential Equations* (Yale U. Press, 1923).
17. W. S. Cleveland and S. J. Devlin, "Locally-weighted regression: an approach to regression analysis by local fitting," J. Am. Stat. Assoc. **83,** 596–610 (1988).
18. H. W. Engel, M. Hanke, and A. Neubauer, *Regularization of Ill-Posed Problems* (Kluwer, 1996).
19. M. Hanke, "Limitations of the L-curve method in ill-posed problems," BIT **36,** 287–301 (1996).
20. A. B. Bakushinskii, "Remarks on choosing a regularization parameter using the quasi-optimality and ratio criterion," USSR Comput. Math. Math. Phys. **24,** 181–182 (1985).
21. C. R. Vogel, "Non-convergence of the L-curve regularization parameter selection method," Inverse Probl. **12,** 535–547 (1996).
22. T. Regenska, "A regularization parameter in discrete ill-posed problems," SIAM J. Sci. Comput. (USA) **17,** 740–749 (1996).
23. D. M. Allen, "The relationship between variable selection and data augmentation and a method for prediction," Technometrics **16,** 125–127 (1974).
24. P. E. Gill, W. Murray, and M. H. Wright, *Practical Optimization* (Academic, 1986).